TECHNICAL MEMORANDUM

259

An explicit low resolution extended Kalman filter: Implementation and preliminary experimentation

M. Ehrendorfer and F. Bouttier

Research Department

September 1998 (SAC Paper)

European Centre for Medium-Range Weather Forecasts
Europäisches Zentrum für mittelfristige Wettervorhersage
Centre européen pour les prévisions météorologiques à moyen

An Explicit Low-resolution Extended Kalman Filter: Implementation and Preliminary Experimentation

Martin Ehrendorfer and François Bouttier

1. Introduction

This paper describes preliminary work on the implementation of an explicit extended Kalman filter (EKF). This EKF is explicit in the sense that it is unsimplified in terms of propagating in time analysis and forecast error covariance matrices. In view of the computational cost involved, carrying these matrices in unsimplified form mandates implementing the EKF at low model resolution; as a consequence, the resolution of the EKF described here is taken as spectrally triangular at total wavenumber 21, with three vertical levels (i.e., T21L3).

Exercising an EKF over time leads potentially to the assessment of analysis error covariance matrices, denoted P^a, that contain the second-moment information for assimilated atmospheric states (see, Bouttier 1996). Naturally, these error covariances become flow dependent. In a predictability context, knowledge about such flow-dependent P^a allows one to study the flow-dependent growth of analysis errors. In particular, P^a may in turn be used for the generation of initial perturbations in ensemble prediction. In a data assimilation context, the short-term evolved P^a may lead to improved, and flow-dependent, background error covariance statistics in an EKF data assimilation cycle.

Two alternative approaches to the low-resolution explicit EKF, as described here, are presently being studied: in the context of the *simplified Kalman filter (SKF)*, described by, for example, Rabier et al. (1997), a high-resolution assimilating model is used, necessitating approximations to be made in the representation of P^a and the associated background error statistics (i.e., the EKF equations are approximated). Thus, the SKF produces an approximation to the covariance matrix of background errors while maintaining high model resolution. A detailed description of the approach taken in the SKF is given in the companion paper by Fisher (1998). The SKF clearly possesses the potential for operational implementation, whereas such operational implementation for an explicit Kalman filter will most likely remain unachieveable. Studying in parallel versions of the SKF and the explicit low-resolution EKF may be expected to provide insight into well-performing configurations of the Kalman filter for possible operational implementation.

In the context of the *ensemble Kalman filter*, described by Houtekamer and Mitchell (1998), an ensemble of analyses is computed (from an ensemble of perturbed observations), that is interpreted as a sample consistent with P^a, which is subsequently evolved in time with the assimilating model. Note that this latter approach requires the analysis step to be inexpensive enough so that it can be repeated several times in order to form the ensemble of analyses.

The *analysis step* of the EKF described here is carried out at resolution T21L3 within the three-dimensional variational (3DVAR) data assimilation scheme as implemented in the ECMWF Integrated Forecasting System (IFS). The EKF *prediction step* is carried out with quasigeostrophic (QG) dynamics. The resulting filter is therefore referred to as QG/EKF. The implementation of the QG/EKF, as well as results from preliminary experiments are discussed here. These preliminary results indicate that with global conventional data, analysis error variances are large over data-void areas (e.g., southern hemisphere), compared to data-rich areas. These geographical differences in $\mathbf{P}^a$ are also reflected by the locations where rapidly amplifying singular vectors based on such analysis error covariance information are found. Background error variances and correlations are substantially different from the standard flow-independent 3DVAR configuration.

2. Implementation of the Extended Kalman Filter

The technical implementation of the QG/EKF described here involves computing the *analysis equation* for the analysis error covariance matrix $\mathbf{P}^a(t_i)$ at time t_i:

$$\mathbf{P}^a(t_i) = (\mathbf{I} - \mathbf{K}_i \mathbf{H}_i)\, \underline{\mathbf{P}^f(t_i)} = \left([\mathbf{P}^f(t_i)]^{-1} + \mathbf{H}_i^T (\mathbf{R}_i)^{-1} \mathbf{H}_i\right)^{-1} \tag{1}$$

as well as the *prediction equation* for the forecast error covariance matrix $\mathbf{P}^f(t_{i+1})$ at time t_{i+1}:

$$\underline{\mathbf{P}^f(t_{i+1})} = \mathbf{M}_i \mathbf{P}^a(t_i) \mathbf{M}_i^T + \mathbf{Q}(t_{i+1}) = (\mathbf{M}_i \mathbf{L}(t_i))\, (\mathbf{M}_i \mathbf{L}(t_i))^T + \mathbf{Q}(t_{i+1}) \tag{2}$$

Here $\mathbf{K}_i$ denotes the Kalman gain, $\mathbf{H}_i$ the linearized observation operator, $\mathbf{R}_i$ the observation error covariance matrix, $\mathbf{M}_i$ the tangent-linear dynamics operator, $\mathbf{L}(t_i)$ the lower-triangular Cholesky factorization of $\mathbf{P}^a(t_i)$, and $\mathbf{Q}(t_{i+1})$ the model-error term. For a more in-depth description of the EKF equations (e.g., for a description of the two equivalent formulations of $\mathbf{P}^a(t_i)$ in eq. (1)), as well as of general aspects of data assimilation, reference is made here to the excellent overviews by Cohn (1997) and Courtier (1997) (see also Jazwinski, 1970).

Equations (1) and (2) are computed explicitly as follows. The analysis equation (1) for the analysis error covariance matrix (i.e., the combination of background error covariances $\mathbf{P}^f$ and observation error covariances $\mathbf{R}$), is carried out within the 3DVAR implementation of the IFS at T21L3 resolution. Specifically, the computation of this analysis equation is done by computing explicitly the Hessian (i.e., the matrix of second derivatives) of the 3DVAR cost function, and subsequently using the result that $\mathbf{P}^a(t_i)$ is the inverse of that Hessian. The explicit computation of this Hessian is done by performing n perturbed cost function gradient calculations (n=6292 at T21L3, if all model variables are considered). In-memory storage and explicit inversion of this matrix is necessary and possible on the ECMWF computer system. Note in particular that the standard 3DVAR implementation of the IFS has been modified to allow for using background error covariances $\mathbf{P}^f(t_i)$ different from the standard configuration. Below, this standard configuration is also referred to as static, in contrast to dynamic, because in the standard configuration the background error covariances remain essentially the same (flow-independent) whenever a 3DVAR minimization is carried out; reference is made to Bouttier et al. (1997) for a description of the standard background error covariance specification. Dynamic background error covariances become available from eq. (2), and they are an input to eq. (1) as indicated by the underlining. Note also that the Kalman gain $\mathbf{K}$ and the observation operator $\mathbf{H}$ are never required explicitly since equation (1) is computed by exploiting the equivalence between 3DVAR and the EKF in the linear situation.

The computation of the prediction equation (2) yielding the forecast error covariance matrix (or, the new background) $\mathbf{P}^f(t_{i+1})$ by time-evolving $\mathbf{P}^a$, is carried out by evolving with the QG dynamics tangent-linearly the vorticity analysis error covariances extracted from the inverse of the so-obtained Hessian (eq. (1)). The dynamical model used here has been developed by Marshall and Molteni (1993), and has been correspondingly adapted (e.g., formulation of its tangent-linear version and interfacing with the IFS conventions) for use in eq. (2). The actual computation of eq. (2) proceeds by acting column by column with the tangent-linear QG model operator on the columns of the Cholesky factorization of the analysis error covariance matrix. The new background obtained as the result of eq. (2), as indicated by the underlining, is used in the next computation of the analysis equation (1) within the IFS, completing the analysis/prediction cycle for the second-moment matrices. This tangent-linear integration in eq. (2) is the only point where the QG/EKF relies on the QG dynamics: the linearization starts at an operationally analysed and archived state, and is defined along a QG predicted (e.g., over 6 hours) trajectory. The tangent-linear approximation is highly accurate for the analysis/forecast error levels encountered in the assimilation. A comment on the specification of the model error term $\mathbf{Q}$ is given in the next section.

The QG/EKF is set up with the possibility to cycle continuously over time through a sequence of two scripts, calling each other consecutively as the QG/EKF runs over time and is alternatingly computing eqs. (1) and (2). Note that the QG/EKF does not implement the first-moment equations corresponding to eqs. (1) and (2); a description of these equations can be found, for example, in Courtier (1997) and Cohn (1997). Whenever such states are required within the QG/EKF (e.g., as initial state for the nonlinear QG model integration to subsequently define $\mathbf{M}_i$ in eq. (2)) they are taken as the operationally analysed and archived states. The reason for adopting this hybrid approach is that T21L3 analyses are very likely inferior to the operational high-resolution analyses. More specific details about the technical implementation of the QG/EKF can be found in Ehrendorfer and Bouttier (1998).

3. Preliminary Results

Two initial experiments have been performed with the QG/EKF for the period starting 19971128/00GMT. In both of these experiments, the time interval from t_i to t_{i+1} has been taken to be six hours. At the beginning of each six-hour interval a set of observations entered the assimilation through eq. (1). The observations used in both experiments are horizontal wind, geopotential, temperature, and surface pressure from SYNOP, AIREP, and TEMP. The two experiments are different in the treatment of the model error term $\mathbf{Q}$ (see below and eq. (2)); emphasis is given here on the results of the experiment where $\mathbf{Q}$ has been taken nonzero.

a) Analysis and forecast error covariances

The overall characteristics of the two experiments are illustrated in Fig. 1, showing the traces of the vorticity analysis and forecast error covariance matrices, $\mathbf{P}^a(t_i)$ and $\mathbf{P}^f(t_i)$, respectively as a function of time. At any given time t_i the larger value corresponds to the background $\mathbf{P}^f(t_i)$, the smaller value to $\mathbf{P}^a(t_i)$. The only difference between the two experiments is that in experiment ekf01 (thin curve) the model error term has been taken to be zero, whereas in experiment ekf03 (thick curve) the model error term $\mathbf{Q}$ is nonzero; more specifically, in this case the model error is diagonal in spectral space and time-independent. Its magnitude is designed such that the analysis error covariances stabilize at a specified level. It is obvious from eq. (1) and Fig. 1 that continuously adding observations without model error (ekf01), decreases the overall variance in the analysis error covariance matrix $\mathbf{P}^a$ over time, asymptotically approaching zero. Using the presently highly artificial model-error term prevents the variances to approach zero, as they seem to stabilize at an overall variance level of $1.5 \times 10^{-10}\ s^{-2}$

(this level is approximately half of the overall variance level contained in the background P^f used at the start of the experiment). The choice of this stabilizing level determines the magnitude of Q.

Also included in Fig. 1 are summary results from five Monte Carlo (MC) experiments (see also subsection (c) below), each started at 00GMT of the five days included in the assimilation experiment. In each MC experiment M=5000 nonlinear QG model integrations were carried out over 48 hours. The initial states for these M integrations were generated by sampling from a multivariate normal probability density function (pdf) with the mean taken as the analysed state at 00GMT, and the covariance structure given by P^a valid at that same time as obtained from experiment ekf03. The results of the MC experiments are summarized in Fig. 1 by plotting the traces of the nonlinearly time-evolving covariance matrices. It can be seen that the error grows exponentially at this stage. For reference, Fig. 1 also includes the traces of the 48-hour *tangent-linear* predictions (with QG dynamics) started from the same P^a (large diamonds). The degree of agreement between the nonlinear MC experiments and the tangent-linear predictions shows that the tangent-linear approximation is highly accurate at this time range and for the perturbation sizes implicitly described by the analysis error covariances P^a. Note that the tangent-linear covariance predictions are (slightly) larger than the nonlinear predictions, as is usually found.

Fig. 2 provides information on analysis/forecast error *variances* (diagonal elements of $P^a(t_i)$ and $P^f(t_i)$in physical space) for 19971201/00GMT and 06GMT (corresponding to t=72 and 78 in Fig. 1) at the three model levels of the QG/EKF (experiment ekf03). The same contours and shadings are used at all three model levels and all three panels. The shading is such that increasing density of the shading means going from low to high variances; white within dense (light) shading indicates high (low) values. The heavy contour separates variances above/below $10^{-11}s^{-2}$. Hatched regions occur for variances below that value. Fig. 2 shows that analysis/forecast error variances generally increase with decreasing pressure. The background error variances at 19971201/00GMT (Fig. 2a) reflect the impact of previously used observations (low variances over the continents), as well as the error growth over the previous six-hour interval. Fig. 2b shows the result of computing eq. (1) using the observations at 19971201/00GMT together with $P^f(t_i)$ shown in Fig. 2a. The general feature apparent in these analysis error variances is a reduction in the amount of variance. This reduction is largest over the continents (e.g., North America). Fig. 2c shows the result of applying eq. (2) to $P^a(t_i)$ shown in Fig. 2b; consequently, Fig. 2c is the background (obtained by QG prediction) for the next analysis (i.e., eq. (1)) to be carried out at 19971201/06GMT. From Fig. 2c a slight increase in the overall variance level, compared to Fig. 2b, is apparent. This increase is the combined result of the tangent-linear dynamics and the model error term (see, eq. (2)). Note that the overall level in variance is smaller in Fig. 2c than in Fig. 2a (see also Fig. 1), which is related to the large variance decrease due to the many observations available at 00GMT (i.e., t=72 hours).

Selected off-diagonal information implied by the forecast error covariance matrix valid at 19971201/00GMT (see also Fig. 2a) is shown in Fig. 3 in terms of correlations of three selected points with all other points in the model domain. The location of the points is listed in the legend for Fig. 3. In all three examples, a clear (westward) tilt with height is apparent in these correlation structures. For example, this tilt may be seen in Fig. 3c by tracing with height the negative correlation area that is located over Spain at 800 hPa. Or, in Fig. 3a, it is seen that the positive correlation area is located at 140°E at 800 hPa and at approximately 130°E at 200hPa. This preliminary assessment of the background error covariances obtained in experiment ekf03 indicates that these are substantially different from the static background error specification in two important respects: namely, in terms of spatial variance patterns and vertical correlations.

b) Hessian singular vectors

The results presented in the following concern some preliminary diagnostics of the analysis error covariance matrix $P^a(t_i)$ shown (in terms of its variances) in Fig. 2b (valid for 19971201/00). More specifically, these diagnostics concern the computation of rapidly amplifying perturbation structures initially constrained by P^a (also referred to as Hessian singular vectors). Given P^a, the Hessian singular vectors (SVs) Z_0 are the solution to the eigenproblem:

$$P^a M_\tau^T C^T C M_\tau Z_0 = Z_0 \Lambda \quad \text{with} \quad Z_0^T (P^a)^{-1} Z_0 = I \tag{3}$$

where M_τ is the tangent-linear (QG) model resolvent over the optimization time τ, $C^T C$ denotes a norm to measure the model state, and Λ is the diagonal eigenvalue matrix (see Ehrendorfer, 1998a). The SV set Z_0 evolves over time τ into the eigenstructure of the forecast error covariance matrix (valid at time τ, in the norm $C^T C$; see also, Ehrendorfer and Tribbia 1997). A recent discussion of the properties of Hessian singular vectors computed using analysis-error covariance information in a primitive-equation model may be found in Barkmeijer et al. (1998).

As a first result, Fig. 4 shows the leading Hessian SV computed over $\tau = 48$ hours (with QG dynamics), using P^a (Fig. 2b) as initial constraint, and total energy (= sum of kinetic and available potential energies; see Ehrendorfer 1998b) of the perturbation to describe the norm $C^T C$. This SV is shown at initial (Fig. 4a) and final (Fig. 4b) times, at the three model levels (all SVs plotted here have been normalized to have the same length; contour intervals are the same). The location depicted by the SV shown in Fig. 4a is characterized by two points: first, this location exhibits large analysis error variance (see Fig. 2b), second, this location may also be unstable as the basic state at the beginning of the optimization interval indicates a slight trough right at this position. The amplification of this SV in terms of total energy is 4.3^2. Inspection of this Hessian SV indicates that its amplitude changes strongly in the vertical; however, its location does not.

Fig. 5 shows an amplifying Hessian SV computed over the same 48-hour period as the SV shown in Fig. 4, with the only exception that the static analysis error covariance matrix (as used for vorticity in the IFS/3DVAR; see section 2) was used as the initial constraint. That is, no flow-dependent information is used in the initial constraint in the SV computation. The patterns shown are for the fifth SV (total energy amplification of 5.3^2), since the four higher-ranking SVs are all located in the northern hemisphere in this situation of the static (observation- and flow-independent) initial constraint. As in the case of the SV shown in Fig. 4, the location of nonzero structures associated with this "static" Hessian SV is almost the same at all three model levels. The fact that the static SV grows (slightly) faster (in terms of total energy) than the SV shown in Fig. 4 may be related to the fact that in this case the SV is not constrained (by the structure of P^a) to be located in certain areas (possibly not so active in terms of total energy).

Finally, the SV shown in Fig. 6 has been obtained completely analogously to the SV shown in Fig. 4, except for the application of a northern hemisphere projection in the final (total energy) norm. This projection is such that structures south of 30°N do not contribute to the final total energy of the perturbation in the SV computation. The SV shown here amplifies by a factor of 6.6^2 in terms of total energy (note that in computing this amplification the total energies of the initial and final SV structures are compared without application of the projection operator). At the initial time some nonzero perturbations are still found in the southern hemisphere, probably due to the large analysis error variances in these areas. The final-time structure is located just at the border of the projection area.

c) Spectra and a predictability experiment

Further information on the analysis error covariance matrix valid for 19971201/00GMT obtained in experiment ekf03 (see Figs. 2b, 4, 6) is provided in Fig. 7a in terms of the eigenspectrum of P^a (dashed curve), as well as in terms of its decomposition in terms of the initial SVs Z_0 (solid curve; see also Fig. 4). Spectra are shown here as cumulative fractions (in percent) of total variance; the total variance in this case (the value used for normalization in Fig. 7a) is $1.045 \times 10^{-10} s^{-2}$ (see also Fig. 1). Note that computing the eigendecomposition of the vorticity analysis error covariance matrix P^a implies use of an enstrophy norm. It is noted that 100 eigenvectors (out of the total number of 1449 eigenvectors) of P^a account for 35.93% of the total variance, whereas the reconstruction of P^a through 100 Hessian SVs (out of the total number of 1449 Hessian SVs) allows one to recover 17.23%. This latter reconstruction of P^a uses the observation that if the set of Hessian SVs Z_0 satisfies eq. (3), then it is possible to write P^a in the form:

$$P^a = Z_0 Z_0^T \tag{4}$$

The solid line in Fig. 7a indicates the cumulative fraction of variance accounted for as a function of the number of SVs used in representing P^a, as in eq. (4). Note that the representation (4) depends on the final norm through the Hessian SV computation (3). Note further that the (tangent-linearly) time-evolved counterpart to (4) is the eigendecomposition of the forecast error covariance matrix (in the norm described by C; see also Ehrendorfer (1998a).

The reconstruction of the 48-hour tangent-linearly time-evolved forecast error covariance matrix in terms of the time-evolved Hessian SVs (without application of the final norm) is shown in Fig. 7b (solid curve). The total forecast error variance used for normalization of this curve is in this case $2.60 \times 10^{-10} s^{-2}$ (note that this is also the value of the diamond plotted at $t = 120$ hours in Fig. 1). Comparison of this value with the initial value of $1.045 \times 10^{-10} s^{-2}$ (see above) leads to an error-doubling time of these small errors (assuming exponential error growth - which is quite a good approximation) of approximately 36 hours (for the vorticity variances). Note that this error-doubling time represents an error-doubling time based on the QG dynamical model used also in eq. (2). In the context of the solid curve in Fig. 7b it is noted that 100 time-evolved Hessian SVs account for 55.46% of the total final variance.

The nonlinearly obtained (through an MC experiment, see also thin curve in Fig. 1 originating at t =72 hours) equivalent to the solid curve in Fig. 7b is shown as the dashed curve in Fig. 7b. More specifically, this dashed curve is the cumulative eigenspectrum of the nonlinearly obtained forecast error covariance matrix (normalized by the total final *nonlinearly predicted* variance of $2.45 \times 10^{-10} s^{-2}$). The similarity of both curves in Fig. 7b is a strong indication that the vorticity variances implied by P^a shown in Fig. 2b are small enough so that perturbation error growth - of perturbations consistent with this P^a - can be described by tangent-linear dynamics over 48 hours. In addition, as mentioned above, these tangent-linear dynamics are such that the overall error amplifies exponentially, with the above-mentioned error-doubling time of approximately 1.5 days (for variances). Note that in the time-evolved covariance structure 100 time-evolved SVs account for about 55.46% of the total variance (solid curve in Fig. 7b; see above). Since this fraction is considerably larger than the comparable eigenspectrum fraction of 35.93% in the analysis error covariance matrix (see above), this result might be an indication that forecast error covariance spectra are (maybe in general) steeper than analysis error covariance spectra (compare solid curve in Fig. 7b with dashed curve in Fig. 7a).

In a preliminary predictability experiment, three 96-hour MC experiments (each with M=5000 members) were carried out from the initial state 19971201/00GMT. The difference between the three experiments was the degree of completeness in describing the initial analysis error covariance matrix $\mathbf{P}^a$. In the first two experiments $\mathbf{P}^a$ was only described through the first 100 (500) Hessian SVs according to eq. (4). In the third experiment the full $\mathbf{P}^a$ (from experiment ekf03 valid at 19971201/00GMT) was supplied (the generation of the initial ensemble members was again performed by sampling from a multivariate normal pdf, see section 3a). The results are shown in terms of predicted variance fields at 800 hPa in Fig. 8. It is apparent from a comparison of Figs. 8b, c that in terms of predicted variances there is very little gain obtainable by supplying all Hessian SVs, rather than just the first 500. Differences are considerably larger, however, when only the first 100 SVs are included in the initial $\mathbf{P}^a$ specification. Reference is again made to Ehrendorfer (1998a), for a discussion on the problem of underestimating the initial variance if eq. (4) is used directly (as has been done here), that is related to the question of how to scale initial perturbations when adding them to a reference state before performing nonlinear model integrations.

4. Conclusions and open questions

The implementation of an explicit extended Kalman filter, as well as some preliminary results obtained from two experiments with the QG/EKF were described. The QG/EKF is technically working, but a number of open questions must be addressed. Potentially, the QG/EKF provides a framework for assessment of Kalman filter configurations proposed for operational use.

One question concerns the issue of how to achieve and/or define realistic overall levels for the analysis and background error covariances. This question is concerned with the level at which the QG/EKF should be expected to stabilize when the assimilation is carried out over several days (see Fig. 1). This question is of particular importance if it is decided to use results from the QG/EKF in specifying background error covariances in a higher-resolution (operational) data assimilation context. This issue concerns at the same time the amount of observations used in the QG/EKF, as well as the magnitude and/or specification of the included model-error term.

Another question concerns reducing the amount of computer time necessary to run the QG/EKF. In the present configuration (specifically, with thinned observations, and the Hessian computation for all variables) the computation of eq. (1) for one synoptic time requires approximately 15 hours of CPU time on one processor of the Fujitsu VPP700. To facilitate and speed up experimentation it will be attempted to reduce this computational cost (e.g., by computing only parts of the 3DVAR cost function Hessian). However, when implementing this strategy it will be necessary to study the information loss in $\mathbf{P}^a$ when it is obtained through this computationally cheaper approach.

A proposed extension of the QG/EKF concerns updating the tangent-linear dynamics operator in eq. (2) (which presently is QG dynamics) by a T21L3 version of linearized primitive-equation (PE) dynamics. This extension appears to be conceptually straightforward, but requires additional technical work and possibly tuning of the T21L3 PE dynamics. This approach would lead to a T21L3/PE/EKF at very little additional CPU and memory costs and probably much more realistic predictions for $\mathbf{P}^f$. In the present QG/EKF implementation, the QG dynamics operate only on the vorticity part of $\mathbf{P}^a$ which requires to supplement the background error covariances for the remaining variables at the next observation time by the standard static background error formulation (for details, see, Ehrendorfer and Bouttier 1998). Clearly, improving the accuracy of computing eq. (2) by improving

the dynamics, becomes a rather important issue if information of the EKF should be interfaced with an operational data assimilation cycle.

Further experiments are planned that are aimed at investigating the behaviour of the QG/EKF (and the need for the model-error term) when observations are inserted less frequently (say, every 24 hours), or when more homogeneous data sets are used (not so heavily concentrated over the northern hemisphere continents).

The present implementation of the QG/EKF should be easily adaptable to compute eq. (2) with some approximations; e.g., along the lines of the so-called ensemble Kalman filter. Here, a (small) sample of realizations from $\mathbf{P}^a$, evolved over time, is used to estimate $\mathbf{P}^f$ (see section 1, and Houtekamer and Mitchell 1998; see also, Burgers et al., 1998). In this case, the framework of the QG/EKF would allow for a straightforward and detailed assessment of the properties of the ensemble Kalman filter when compared to an explicit Kalman filter.

It should also be easily possible to implement the ideas of the simplified Kalman filter (see section 1, Fisher 1998, and Rabier et al. 1997) in the context of the QG/EKF with the aim of studying the behaviour of the SKF methodology in the framework of the QG/EKF. Presumably, one aspect here involves computing SVs from an estimated/approximated $\mathbf{P}^a$, and performing the computation of eq. (2) on the basis of these SVs. More specifically, it should easily be possible to investigate the QG/EKF dynamic background error formulations in the so-called control variable space of the IFS, and to study the deviation of this QG/EKF background from the specified static background (which is the identity in the standard IFS/3DVAR configuration). As a next step, one might check where the SKF-approximated background error covariances are found in between these extremes.

Further, using the analysis error covariance matrices $\mathbf{P}^a$ obtained with the QG/EKF in SV-based targeting and predictability studies (see, e.g., Palmer et al. 1998) might provide additional information for the detection of regions sensitive to error growth, as well as evidence for the influence of (certain types of) observations on such regions. In such targeting studies, the norm operator $\mathbf{C}$ (eq. (3)) is taken to include a projection onto certain areas of interest. Among various questions, one might, for example, address the question of how forecast error projects onto time-evolved SVs computed on the basis of $\mathbf{P}^a$, compared to time-evolved SVs based on static analysis covariances.

Finally, in terms of ensemble prediction, it is possible with the $\mathbf{P}^a$ matrices obtained with the QG/EKF to restrict the initial covariance information used in ensemble prediction to a low-rank approximation of $\mathbf{P}^a$, and study the differences in time-evolving ensembles originating from such different low-rank approximations (along the lines of eq. (4)). It is conceivable that adding more SVs beyond a certain low-rank approximation of $\mathbf{P}^a$ will not change the time-evolving covariance structure significantly.

REFERENCES

Barkmeijer, J., M.v. Gijzen, and F. Bouttier, 1998: Singular vectors and estimates of the analysis-error covariance metric. Quarterly Journal of the Royal Meteorological Society, Vol 124, 1695-1713.

Bouttier, F., 1996: Application of Kalman filtering to numerical weather prediction. Proceedings 1996 ECMWF Seminar on data assimilation and Workshop on non-linear aspects of data assimilation, 61-90.

Bouttier, F., J. Derber, and M. Fisher, 1997: The 1997 revision of the J_b term in 3D/4D-Var. ECMWF Technical Memorandum No. 240, 54 pp.

Burgers, G., P.J. van Leeuwen, and G. Evensen, 1998: Analysis scheme in the Ensemble Kalman Filter. Monthly Weather Review, Vol 126, 1719-1724.

Cohn, S.E., 1997: An introduction to estimation theory. Journal of the Meteorological Society of Japan, Vol 75, No. 1B, 257-288.

Courtier, P., 1997: Variational methods. Journal of the Meteorological Society of Japan, Vol 75, No. 1B, 211-218.

Ehrendorfer, M., 1998a: Prediction of the uncertainty of numerical weather forecasts: problems and approaches. Proceedings ECMWF Workshop on Predictability, 20-23 October 1997, 27-101.

Ehrendorfer, M., 1998b: Energy norms in the T21L3 Marshall/Molteni quasigeostrophic model. Research Department Memorandum, in preparation.

Ehrendorfer, M., and F. Bouttier, 1998: An explicit low-resolution Extended Kalman Filter based on quasigeostrophic dynamics. ECMWF Technical Memorandum, in preparation.

Ehrendorfer, M., and J.J. Tribbia, 1997: Optimal prediction of forecast error covariances through singular vectors. Journal of the Atmospheric Sciences, Vol 54, 286-313.

Fisher, M., 1998: Development of a Simplified Kalman Filter. Paper for presentation to the ECMWF Scientific Advisory Committee.

Houtekamer, P.L., and H.L. Mitchell, 1998: Data assimilation using an ensemble Kalman filter technique. Monthly Weather Review, Vol 126, 796-811.

Jazwinski, A.H., 1970: Stochastic processes and filtering theory. Academic Press, 376 pp.

Marshall, J., and F. Molteni, 1993: Toward a dynamical understanding of planetary-scale flow regimes. Journal of the Atmospheric Sciences, Vol 50, 1792-1818.

Palmer, T.N., R. Gelaro, J. Barkmeijer, and R. Buizza, 1998: Singular vectors, metrics, and adaptive observations. Journal of the Atmospheric Sciences, Vol 55, 633-653.

Rabier, F., J.-F. Mahfouf, M. Fisher, et al., 1997: Recent experimentation on 4D-VAR and first results from a Simplified Kalman Filter. ECMWF Technical Memorandum No. 240, 42 pp.

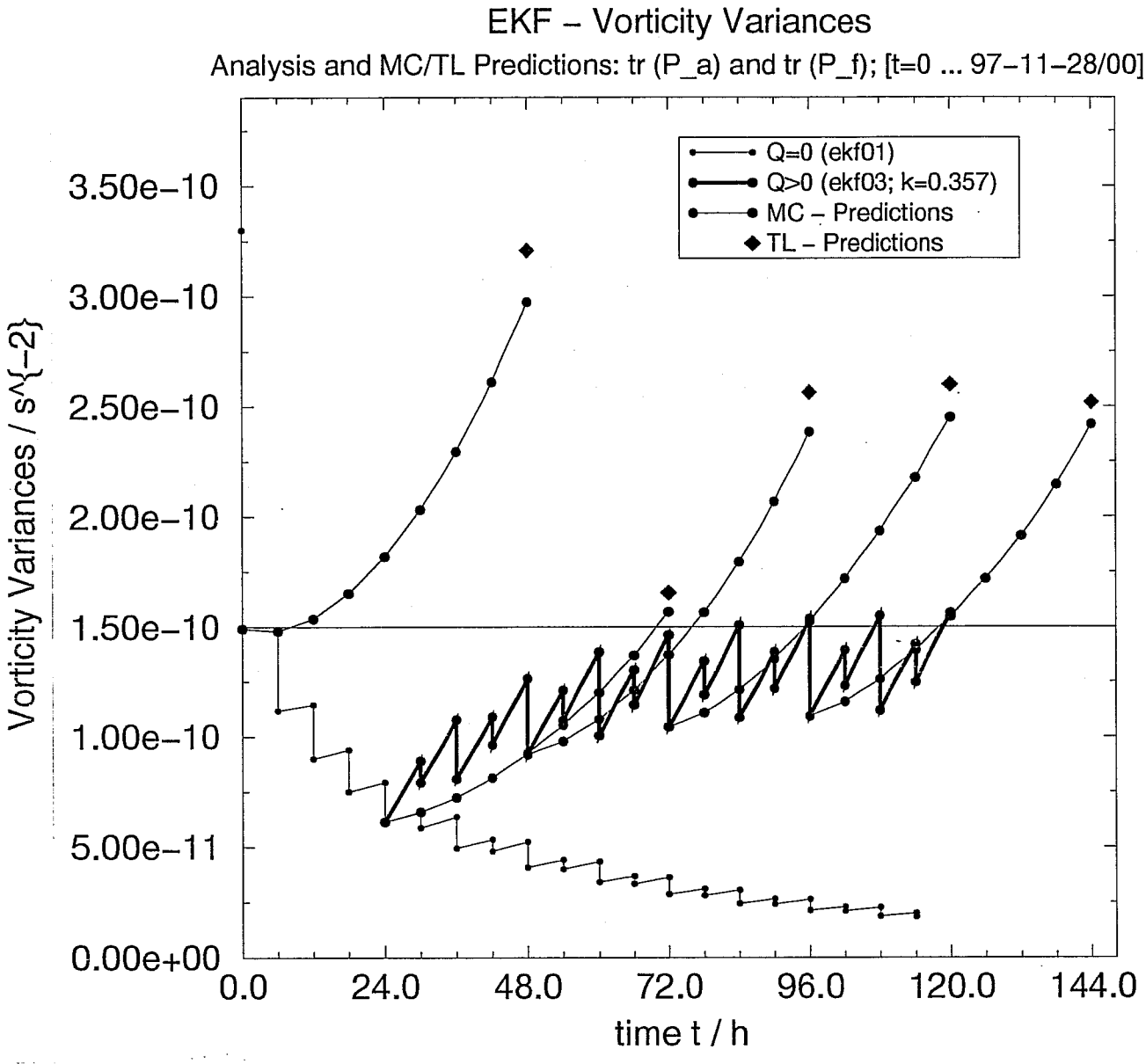

Fig. 1. Overall performance characteristics of the quasigeostrophic Kalman filter. Shown are the traces of the vorticity analysis and forecast error covariance matrices, $P^a(t_i)$ and $P^f(t_i)$, respectively, as a function of time, for two experiments, in units of s^{-2}. Time t=0 corresponds to 19971128/00GMT. The thin curve (labelled Q=0; ekf01) refers to an experiment without model error (see eq. (2)). The thick curve (labelled Q>0; ekf03) refers to an experiment using a simple model error formulation. In both experiments the same observations were assimilated. Experiment ekf01 is initialized by computing eq. (1) using the standard 3DVAR background error formulation. Experiment ekf03 starts at 19971129/00GMT with eq. (1) using the background available for this time from ekf01. The five thin curves originating at 00GMT (labelled MC-predictions) show the traces of the forecast error covariance matrices as obtained from large-ensemble (M=5000) nonlinear Monte Carlo experiments (with QG dynamics) originating from the analysed states and corresponding P^a valid for the particular times. The diamonds plotted at the end of the 48-hour MC predictions indicate the traces of the 48-hour tangent-linearly evolved analysis error covariance matrices, providing information on the accuracy of the tangent-linear approximation.

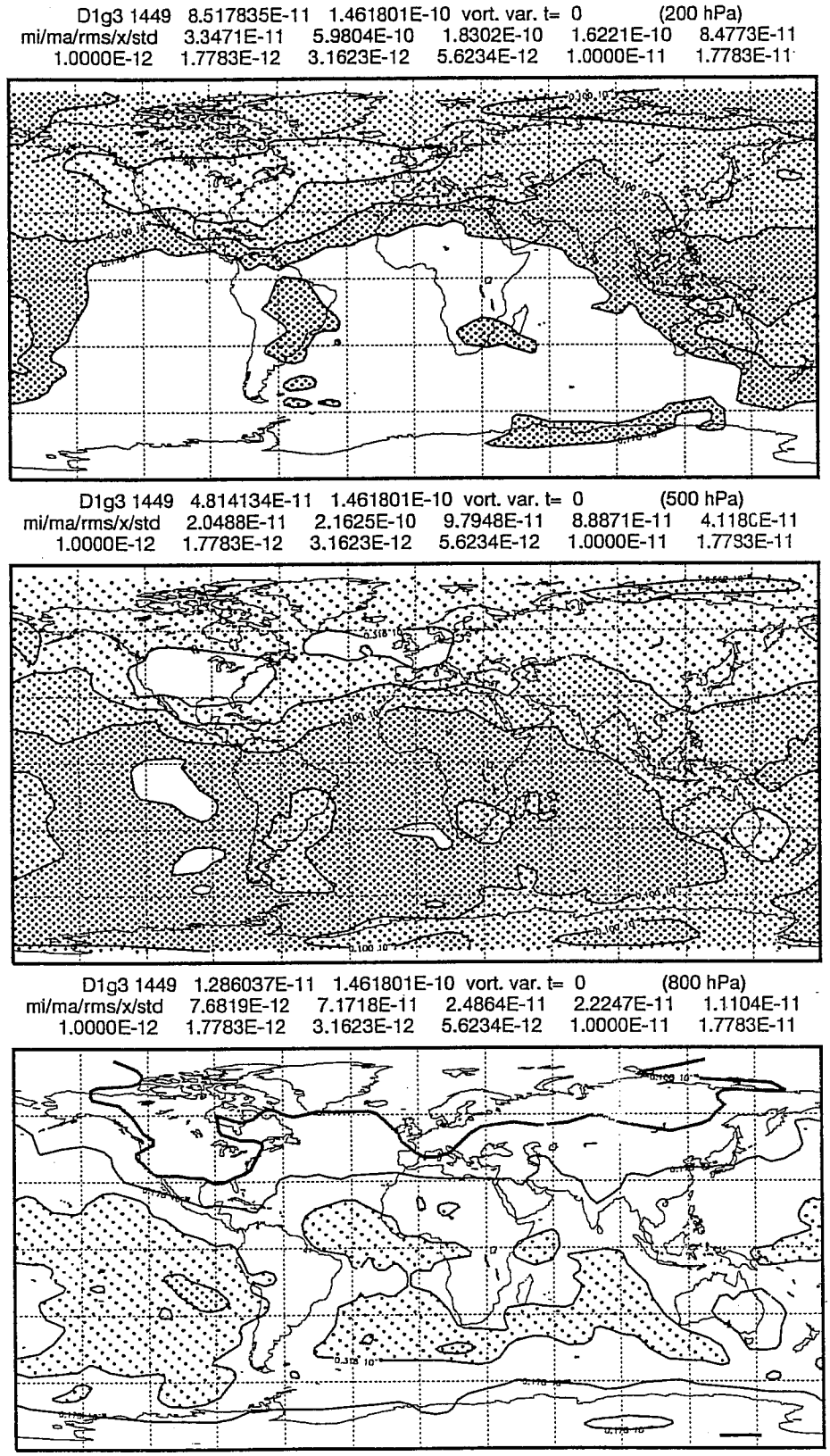

Fig. 2. Vorticity variances at the three model levels (200 hPa, 500 hPa, 800 hPa; from top to bottom) in physical space in units of s^{-2}: (a) P^f at 19971201/00GMT, (b) P^a at 19971201/00GMT, (c) P^f at 19971201/06GMT. The same contours and shading conventions are used in all panels. The heavy contour denotes 10^{-11} s^{-2}. Darker shading corresponds to larger variances, hatching to low variances. Unshaded regions within light (dark) shading indicate low (high) variances.

D1b3 1449 6.123291E-11 1.044930E-10 vort. var. t= 0 (200 hPa)
mi/ma/rms/x/std 4.4916E-12 4.7093E-10 1.4168E-10 1.1654E-10 8.0561E-11
1.0000E-12 1.7783E-12 3.1623E-12 5.6234E-12 1.0000E-11 1.7783E-11

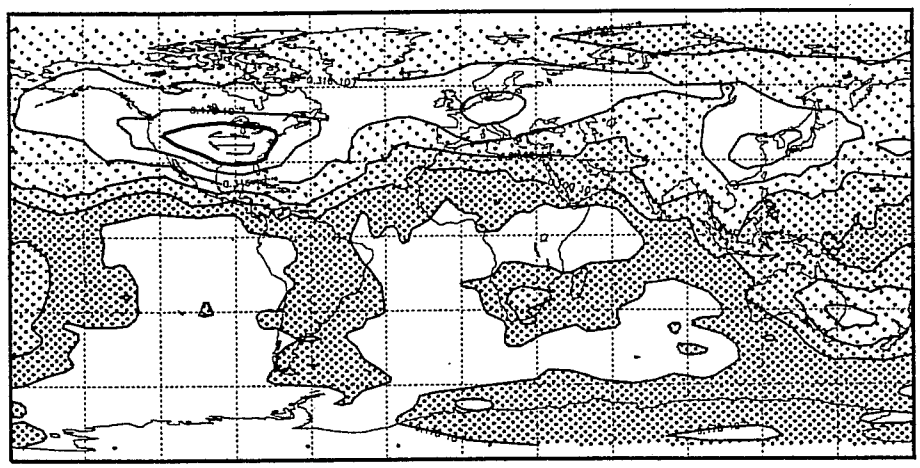

D1b3 1449 3.381966E-11 1.044930E-10 vort. var. t= 0 (500 hPa)
mi/ma/rms/x/std 3.8672E-12 1.7629E-10 7.3255E-11 6.2059E-11 3.8922E-11
1.0000E-12 1.7783E-12 3.1623E-12 5.6234E-12 1.0000E-11 1.7783E-11

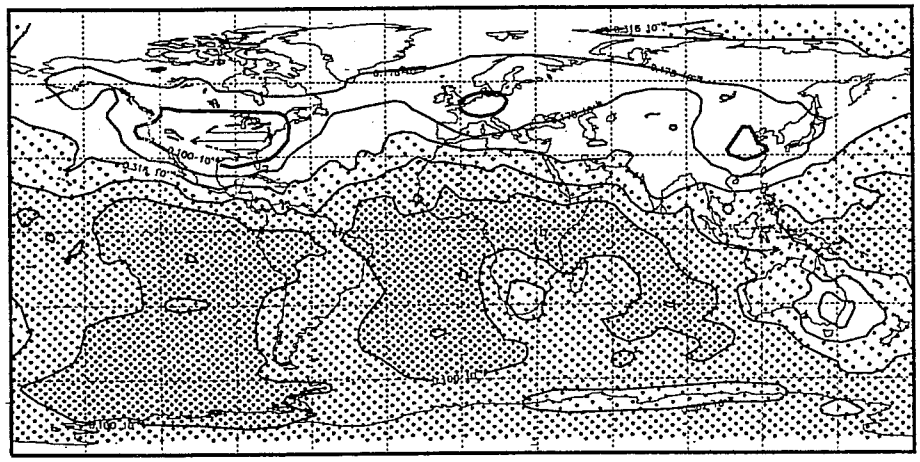

D1b3 1449 9.440445E-12 1.044930E-10 vort. var. t= 0 (800 hPa)
mi/ma/rms/x/std 2.4480E-12 5.1289E-11 1.8719E-11 1.6062E-11 9.6124E-12
1.0000E-12 1.7783E-12 3.1623E-12 5.6234E-12 1.0000E-11 1.7783E-11

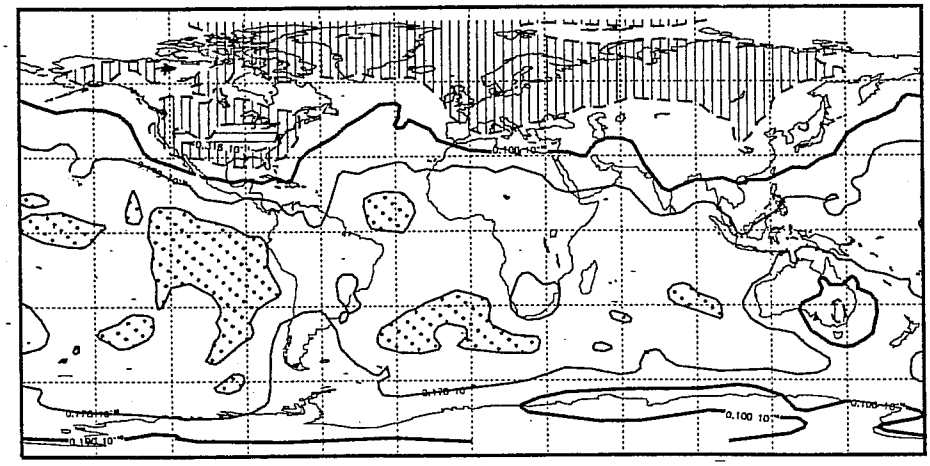

Fig. 2. continued; panel (b).

D2g3 1449 7.881129E-11 1.343972E-10 vort. var. t= 0 (200 hPa)
mi/ma/rms/x/std 3.2399E-11 5.6378E-10 1.7158E-10 1.4901E-10 8.5061E-11
1.0000E-12 1.7783E-12 3.1623E-12 5.6234E-12 1.0000E-11 1.7783E-11

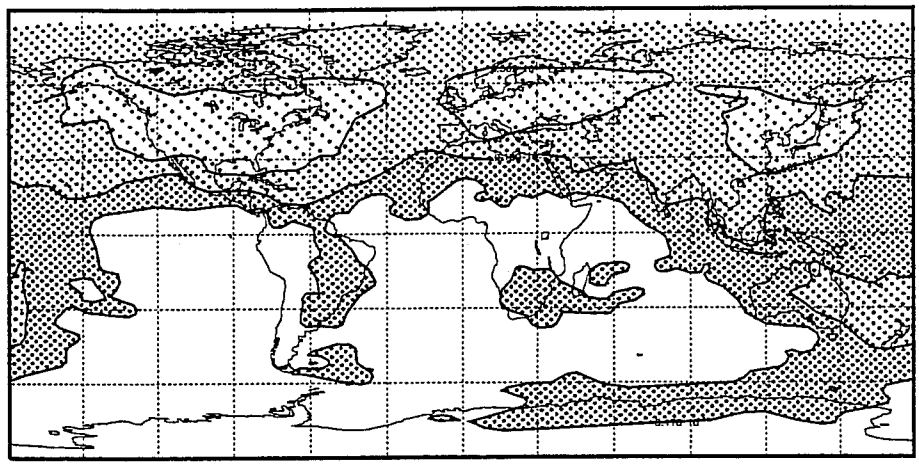

D2g3 1449 4.355167E-11 1.343972E-10 vort. var. t= 0 (500 hPa)
mi/ma/rms/x/std 1.9795E-11 2.0853E-10 9.0091E-11 8.0032E-11 4.1366E-11
1.0000E-12 1.7783E-12 3.1623E-12 5.6234E-12 1.0000E-11 1.7783E-11

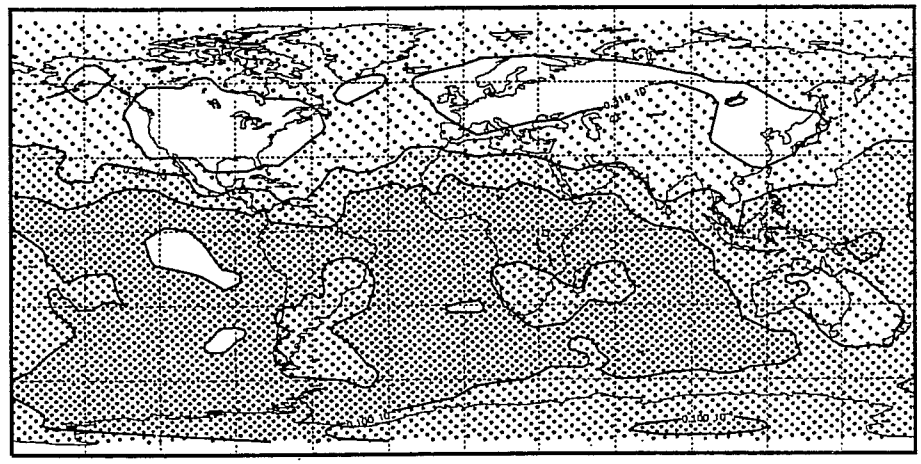

D2g3 1449 1.203428E-11 1.343972E-10 vort. var. t= 0 (800 hPa)
mi/ma/rms/x/std 7.1694E-12 6.4912E-11 2.3441E-11 2.0764E-11 1.0878E-11
1.0000E-12 1.7783E-12 3.1623E-12 5.6234E-12 1.0000E-11 1.7783E-11

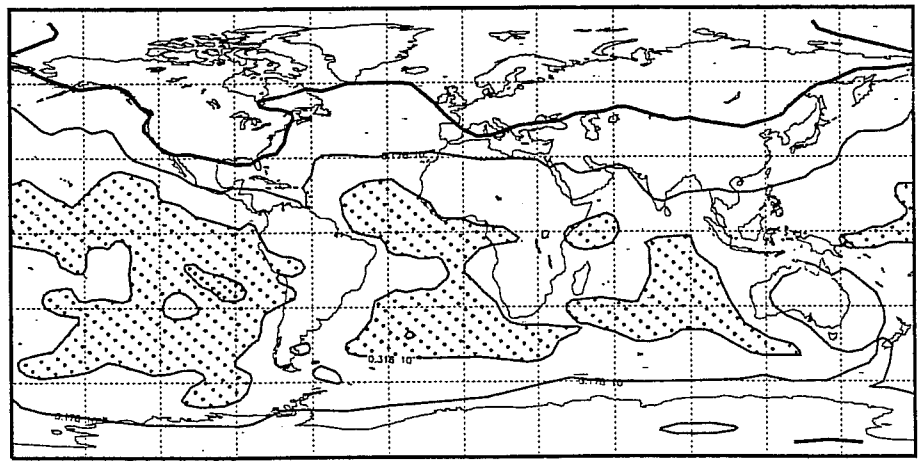

Fig. 2. continued; panel (c).

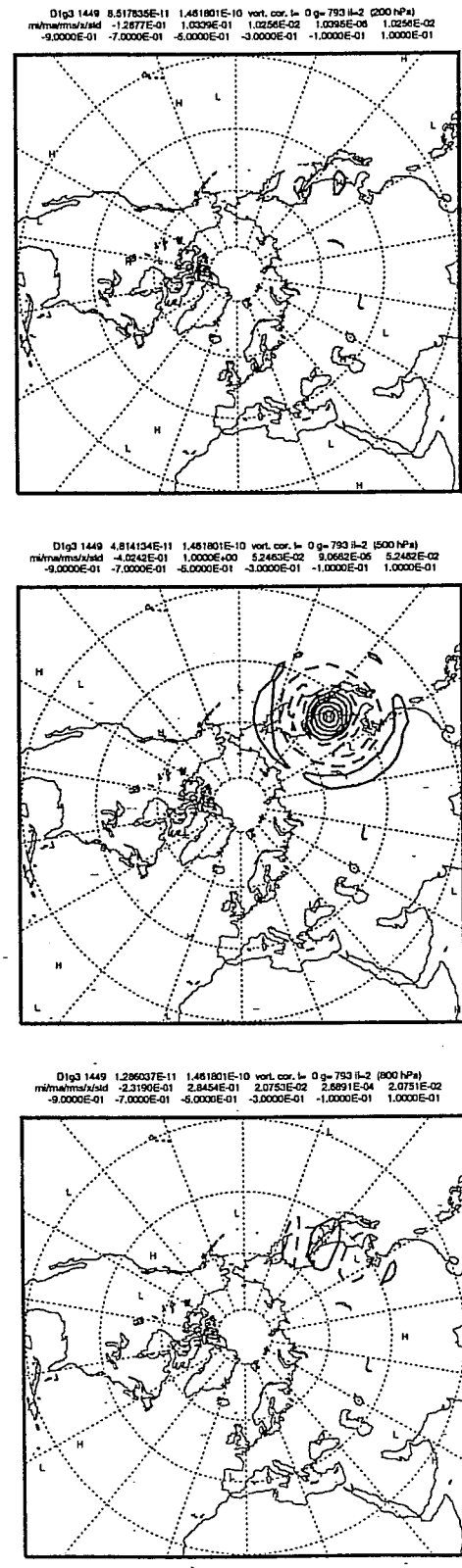

Fig. 3. Selected off-diagonal information for the background error covariance matrix used in experiment ekf03 at 19971201/00GMT, in terms of correlation structures implied by P^f (valid for 19971201/00GMT) (see Fig. 2a) of three selected points with all other points on the globe at the three model levels (northern hemisphere shown only; model levels shown from top to bottom). The three selected points are all located at the 500 hPa model level, and (a) on the east coast of Asia (135°E, 45°N), (b) in the northern Pacific (180°E, 30°N), (c) in the northern Atlantic (30°W, 45°N). Note the westward tilt with height in the correlation structures. Contour interval is 0.2.

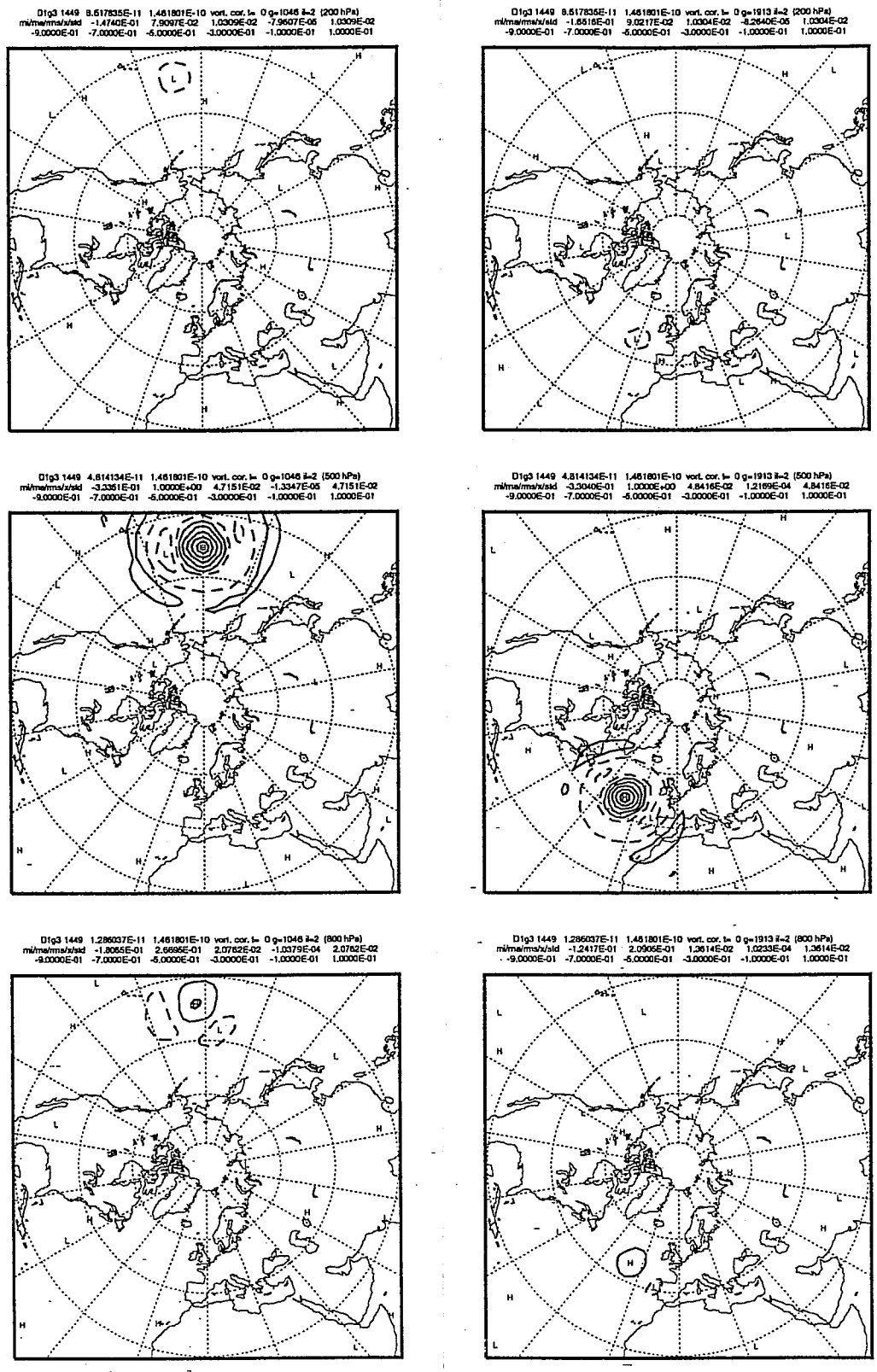

Fig. 3. continued; left: panel (b); right: panel (c).

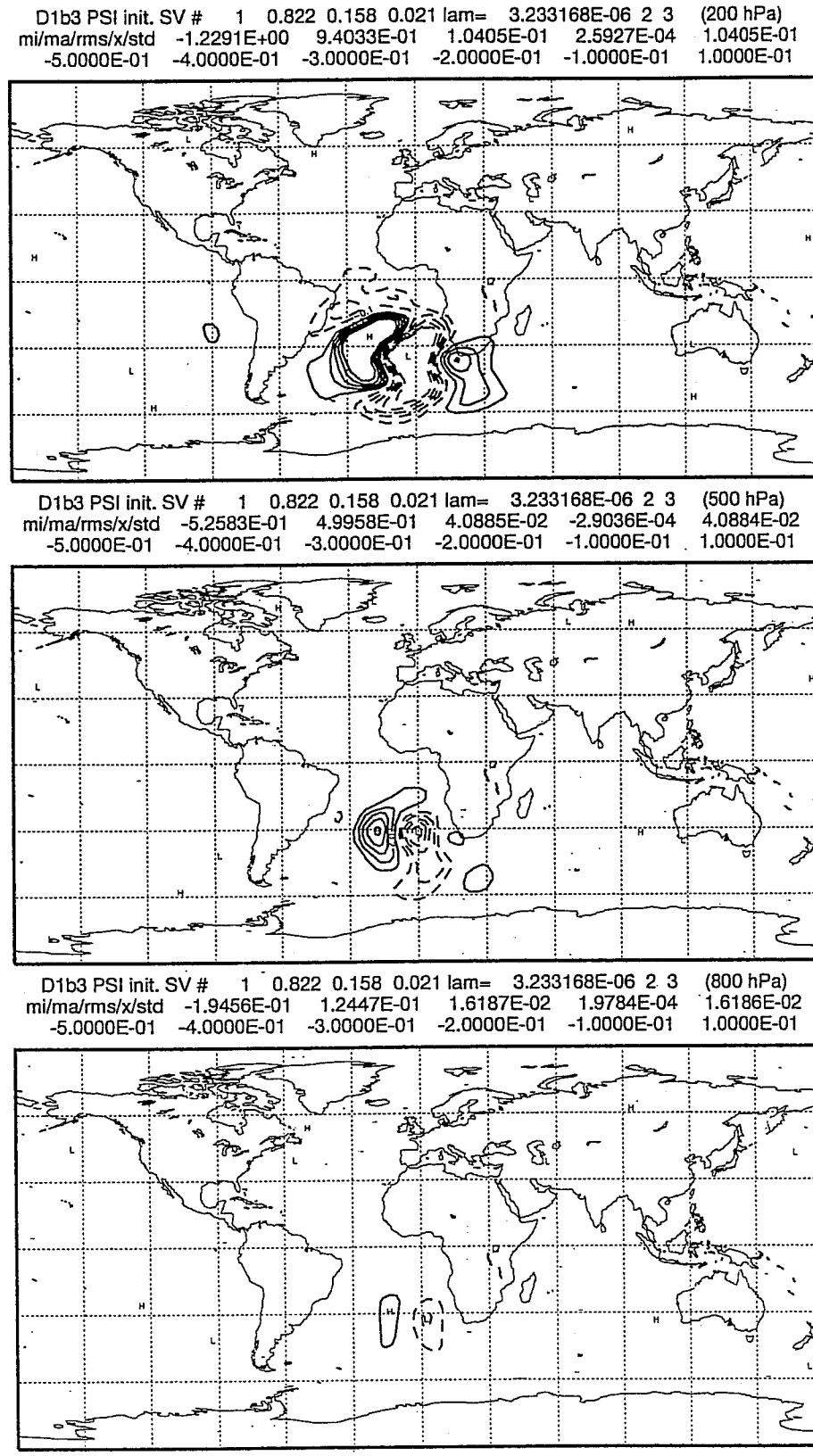

Fig. 4. The leading Hessian singular vector at (a) initial time, (b) final time at the three model levels, computed with quasigeostrophic dynamics over the 48-hour optimization interval from 19971201/00GMT to 19971203/00GMT. The initial constraint is defined by P^a (valid for 19971201/00GMT) (see Fig. 2b), the final norm is total energy. The singular vector is scaled to the same length at both initial and final times, and is plotted in terms of a streamfunction perturbation. The same contour interval of 0.1 is used in all panels.

D1b3 PSI final SV # 1 0.585 0.336 0.079 KEa= 2.097E+01 TEa 1.906E+01 (200 hPa)
mi/ma/rms/x/std -7.2497E-01 7.8432E-01 8.2374E-02 -7.0954E-04 8.2370E-02
-5.0000E-01 -4.0000E-01 -3.0000E-01 -2.0000E-01 -1.0000E-01 1.0000E-01

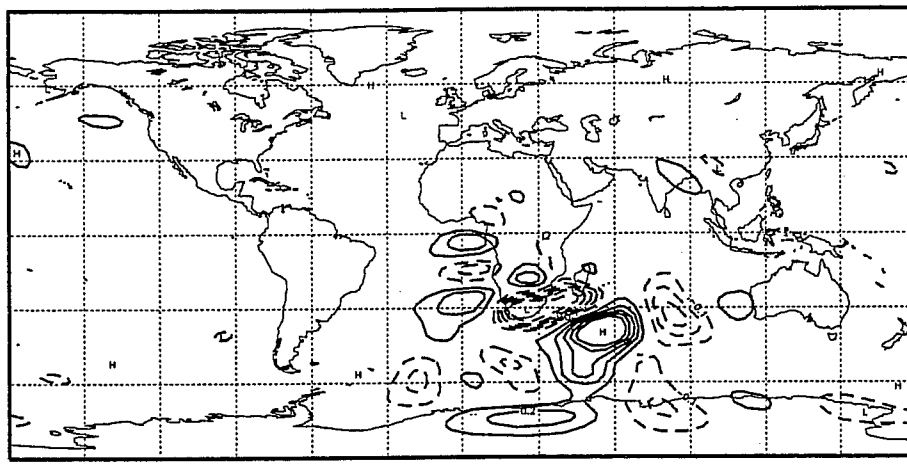

D1b3 PSI final SV # 1 0.585 0.336 0.079 KEa= 2.097E+01 TEa 1.906E+01 (500 hPa)
mi/ma/rms/x/std -4.9483E-01 9.4585E-01 6.9103E-02 -1.1025E-03 6.9095E-02
-5.0000E-01 -4.0000E-01 -3.0000E-01 -2.0000E-01 -1.0000E-01 1.0000E-01

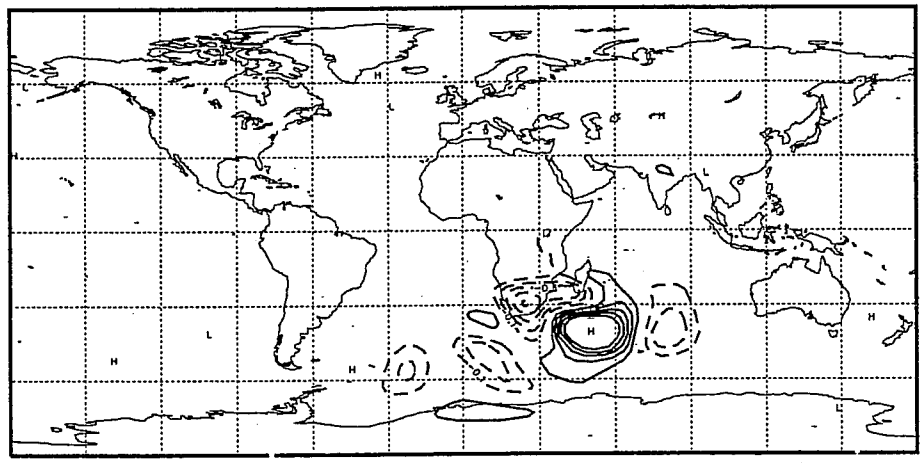

D1b3 PSI final SV # 1 0.585 0.336 0.079 KEa= 2.097E+01 TEa 1.906E+01 (800 hPa)
mi/ma/rms/x/std -2.5824E-01 4.7189E-01 4.0745E-02 -1.0845E-03 4.0731E-02
-5.0000E-01 -4.0000E-01 -3.0000E-01 -2.0000E-01 -1.0000E-01 1.0000E-01

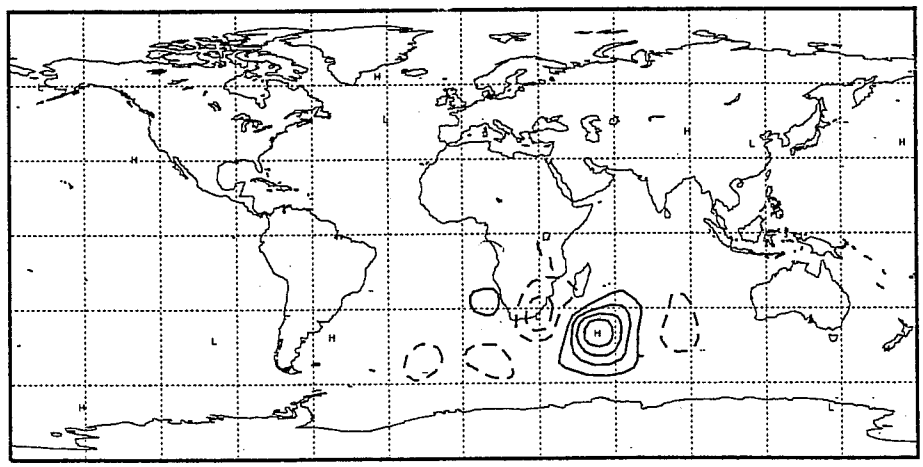

Fig. 4. continued; panel (b).

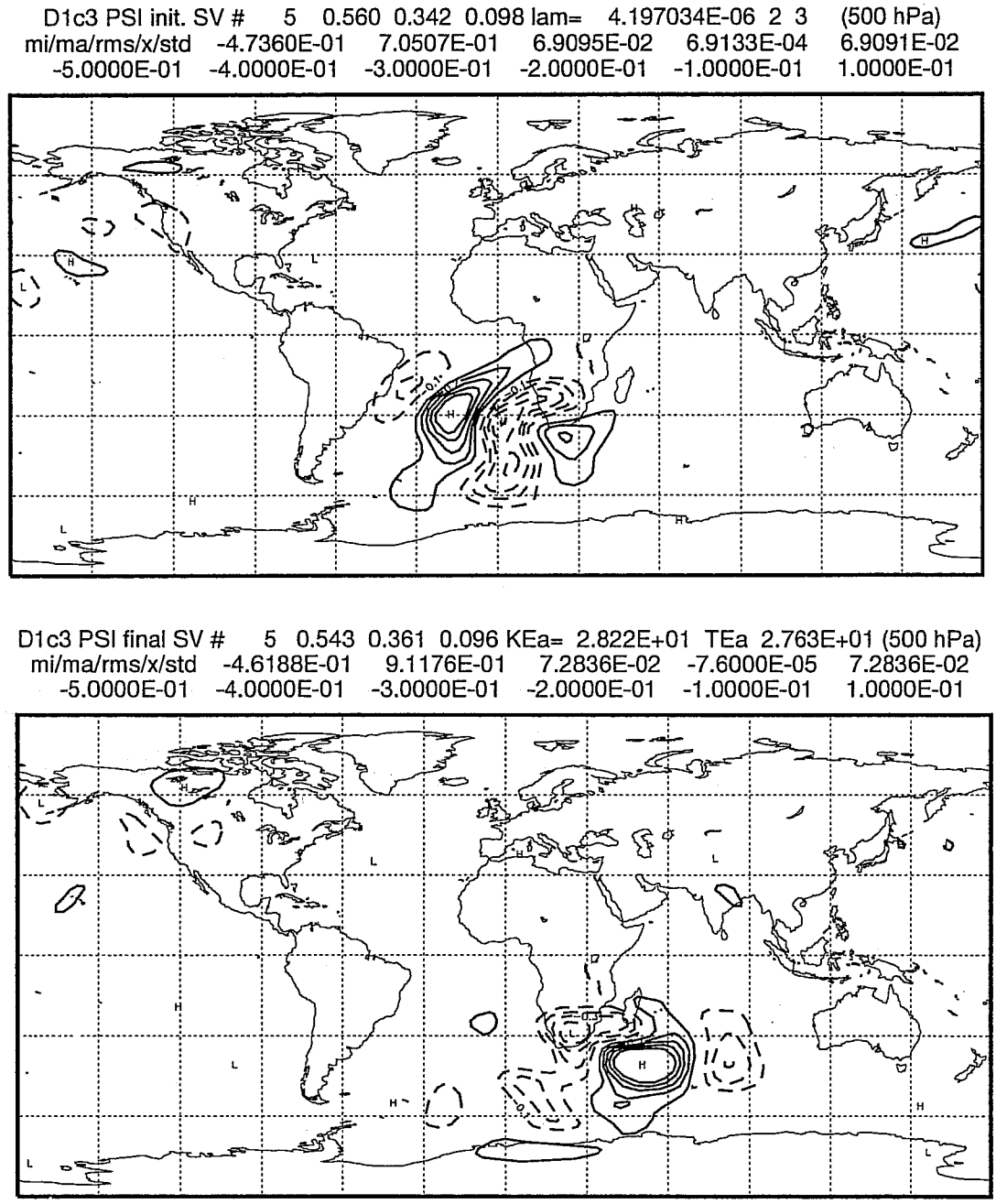

Fig. 5. As in Fig. 4, except for the initial constraint defined through the standard 3DVAR background formulation. The Hessian singular vector shown is not the leading one, but the one matching Fig. 4. Only the 500 hPa structures are shown for initial time (top), and final time (bottom), as the location of nonzero structures is (almost) the same at the other model levels.

D1d3 PSI init. SV # 1 0.450 0.483 0.067 lam= 7.907097E-07 2 4 (500 hPa)
mi/ma/rms/x/std -3.8718E-01 4.2612E-01 6.9715E-02 4.9500E-04 6.9713E-02
-5.0000E-01 -4.0000E-01 -3.0000E-01 -2.0000E-01 -1.0000E-01 1.0000E-01

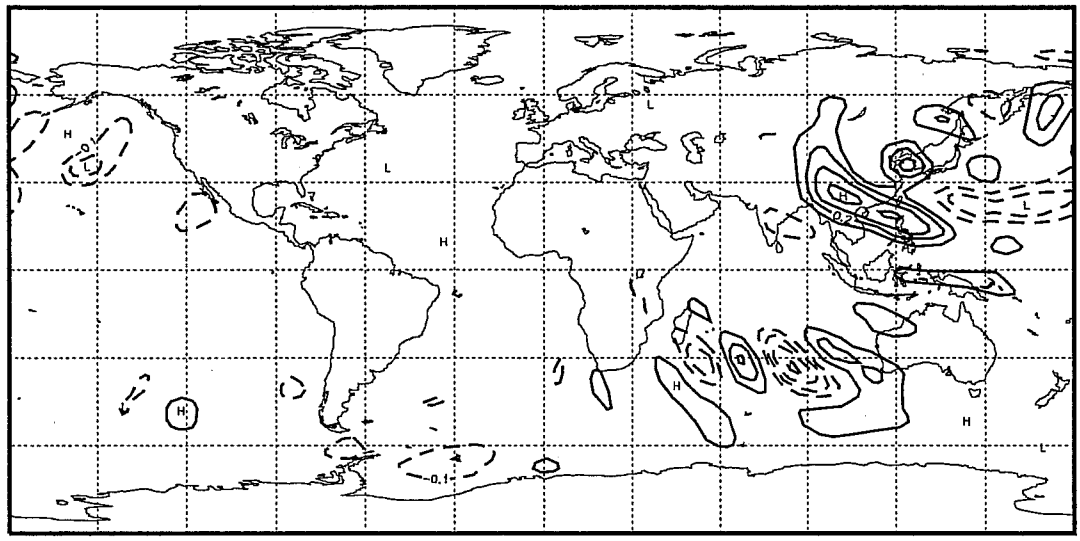

D1d3 PSI final SV # 1 0.416 0.386 0.199 KEa= 6.442E+01 TEa 4.326E+01 (500 hPa)
mi/ma/rms/x/std -5.0148E-01 1.0863E+00 7.5880E-02 -8.6752E-04 7.5875E-02
-5.0000E-01 -4.0000E-01 -3.0000E-01 -2.0000E-01 -1.0000E-01 1.0000E-01

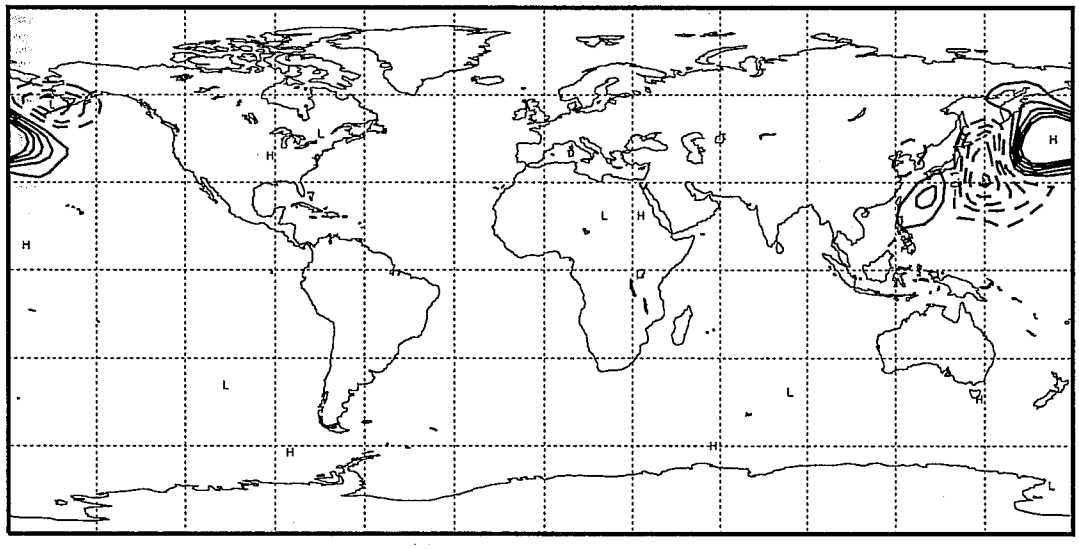

Fig. 6. As in Fig. 4, except for including a northern hemisphere projection in the final (total energy) norm (i.e., zero weight is given to structures south of 30°N). Only the 500 hPa structures are shown for initial time (top), and final time (bottom).

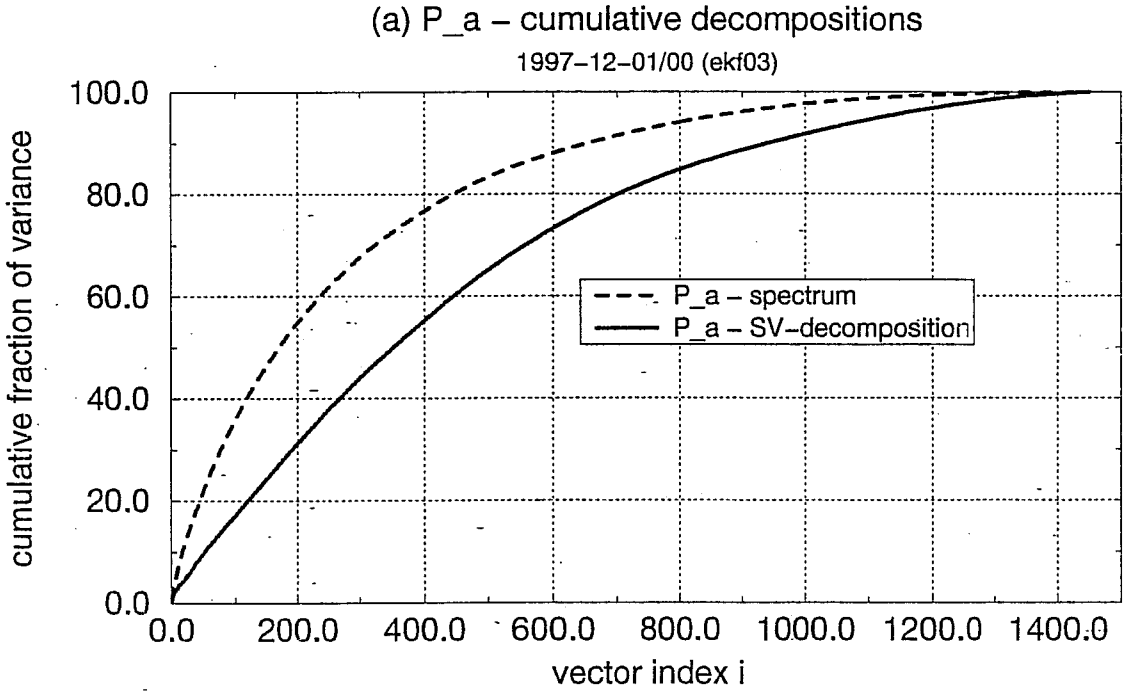

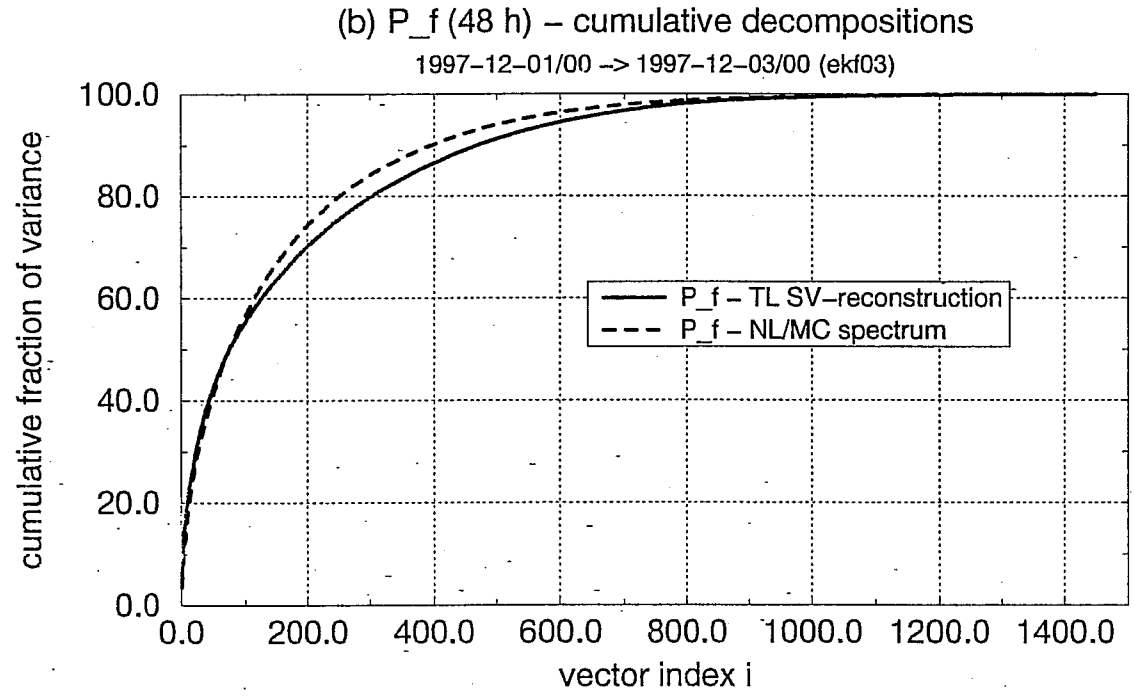

Fig. 7. Cumulative decompositions of vorticity analysis (P^a, valid for 19971201/00GMT) and forecast error covariance matrices (48-hour prediction valid for 19971203/00GMT), in terms of cumulative fractions of variance (in percent), as a function of the number of vectors used in the decomposition. Panel (a) shows the spectrum of P^a (dashed curve), as well as its decomposition (see eq.(4)) in terms of the initial-time 48-hour-optimized Hessian singular vectors (solid curve; computed with total energy at the final time). Panel (b) shows the spectrum of the nonlinearly obtained forecast error covariance matrix (dashed line; MC experiment with M=5000), as well as the reconstruction of the forecast error covariance matrix through the tangent-linearly evolved (i.e. final-time) Hessian singular vectors (solid curve). Note that the total variances used for the normalization in computing the cumulative fractions are the same for both curves in panel (a), but are slightly different in panel (b), due to the influence of nonlinearity.

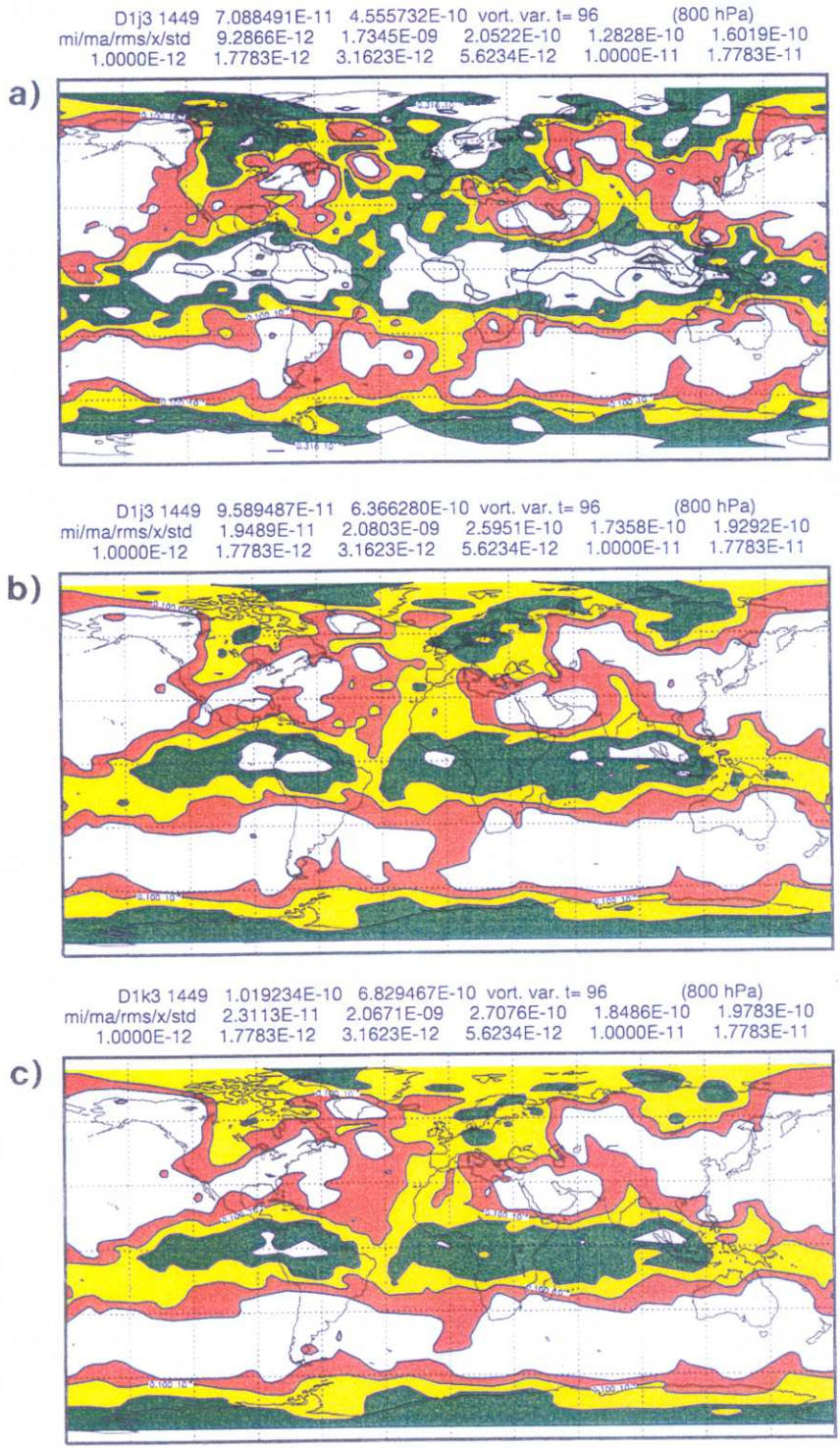

Fig.8. Results from a 96-hour nonlinear large-ensemble M=5000 Monte Carlo experiment (with quasigeostrophic dynamics). Shown is the forecast error covariance matrix valid for 19971205/00GMT at the 800 hPa model level for three experiments differing only in the specification of the analysis error covariance matrix (determining the initial probability density function). In panel (a) the specification of the analysis error covariance matrix was (according to eq.(4)) restricted to 100 initial-time 48-hour-optimized Hessian singular vectors (accounting for 17.23% of the total initial variance; see solid curve in Fig. 7a); in panel (b) 500 of these Hessian singular vectors were used (accounting for 65.22% of the total initial variance; see solid curve in Fig. 7a). In panel (c) the complete matrix P^a (valid for 19971201/00GMT) was used to define the initial probability density function in the MC-experiment. Note that the forecast time in the MC-experiment is twice the Hessian singular vector optimization time. Note further the close correspondence between panels (b) and (c). The contouring convention is the same as in Fig. 2; the colours green/yellow/red have the same meaning as the light/medium/heavy shading in Fig. 2.